

## Review Article

Patrick Helfenstein\*, Iacopo Mochi, Rajendran Rajeev, Sara Fernandez and Yasin Ekinci

# Coherent diffractive imaging methods for semiconductor manufacturing

<https://doi.org/10.1515/aot-2017-0052>

Received August 9, 2017; accepted September 21, 2017; previously published online December 4, 2017

**Abstract:** The paradigm shift of the semiconductor industry moving from deep ultraviolet to extreme ultraviolet lithography (EUVL) brought about new challenges in the fabrication of illumination and projection optics, which constitute one of the core sources of cost of ownership for many of the metrology tools needed in the lithography process. For this reason, lensless imaging techniques based on coherent diffractive imaging started to raise interest in the EUVL community. This paper presents an overview of currently on-going research endeavors that use a number of methods based on lensless imaging with coherent light.

**Keywords:** actinic inspection; coherent diffractive imaging; extreme ultraviolet (EUV); lensless imaging; mask inspection; ptychography; wafer inspection.

## 1 Introduction

Semiconductor technology as the foundation of the digital revolution has transformed the way we live, think, consume, and communicate and will continue to do so with increasing pace in the next decades. The semiconductor industry has continuously evolved in making more compact and faster integrated circuits at decreasing cost as was predicted by Moore's law. This has been enabled by steady downscaling of feature sizes through the advancement of lithographic techniques as well as new device design concepts. The roadmap of the semiconductor industry envisions further downscaling and devices extending into the third dimension. These ambitious plans, however, face tremendous challenges in manufacturing, processing, metrology and material science. In

high-volume manufacturing, optical lithography has been the dominant patterning method due to its high resolution and throughput capability. In order to enable further shrinking of feature sizes, the semiconductor industry is aiming to introduce extreme ultraviolet lithography (EUVL) at a wavelength of  $\lambda = 13.5$  nm, which is one order of magnitude smaller than the 193 nm currently being used in deep ultraviolet lithography (DUV).

With this downscaling, metrology is also becoming increasingly challenging. Being one of the key technologies in the semiconductor manufacturing process, metrology is used in many steps of the fabrication pipeline to monitor and control various structural parameters. It can be divided into two main sections:

1. on-wafer metrology
2. mask metrology

Thereby, on-wafer metrology describes the quality assessment and failure analysis of a plethora of nanostructures, ranging from thin films and patterned photoresists to integrated devices. The latter, being a three-dimensional (3D) structure, can usually only be imaged by destroying the device. In contrast, mask metrology concerns itself with the verification of designed structures and the fabrication of defect-free masks, an essential step during fabrication as the patterns on a single mask will be copied thousands of times during exposure. It is therefore of utmost importance that all masks are free of defects that could lead to device failure on the patterned wafer. In fact, one of the main challenges of EUVL is realizing defect-free reflective masks.

As extreme ultraviolet (EUV) light is strongly absorbed by all matter, masks and all optical components used in EUVL have to be coated with reflective multi-layer thin-film structures consisting of 40 or more alternating silicon and molybdenum layers with thicknesses tuned to maximize the Bragg reflection of the incident light at a predefined angle of incidence. For EUV light at 13.5-nm wavelength (92 eV photon energy) with a  $6^\circ$  angle of incidence (AOI), these Mo/Si multi-layers reach a reflectivity of up to 70%. Although different metrology tools such as scanning electron microscopy (SEM), atomic force microscopy (AFM), and DUV microscopy provide some valuable

\*Corresponding author: Patrick Helfenstein, Paul Scherrer Institute, Villigen, Switzerland, e-mail: patrick.helfenstein@psi.ch

Iacopo Mochi, Rajendran Rajeev, Sara Fernandez and Yasin Ekinci: Paul Scherrer Institute, Villigen, Switzerland

information, only actinic inspection, i.e. metrology with EUV light at the aforementioned AOI, which is identical to the illumination conditions in manufacturing, enables the true characterization of the defects [1]. This requires the development of a reflective imaging technology for the assessment of the defects of multi-layer masks. In particular, the defects that are buried within or under the multi-layer cannot be detected with conventional methods. For this reason, actinic inspection methods are of great importance and considered indispensable for the commercialization of EUVL.

As mentioned above, the difficulty in realizing EUV defect inspection with well-established tools and methods is due to the fact that EUV radiation is strongly absorbed by almost all materials. This makes it necessary to arrange all the optical elements in a reflective setup and to switch to a reflective mask. The change from transmission to reflection has multiple implications. First of all, the reticle can no longer be treated as a two-dimensional object. The height of the absorber pattern and  $6^\circ$  AOI of the EUV beam leads to 3D effects like shadowing and pitch-dependent focal plane variations [2], which affect the aerial image and projection on the wafer and have to be taken into account at the mask design stage. The ability of newer-generation EUV scanners to illuminate the mask with an arbitrarily shaped pupil alleviates this problem to a certain degree, but the fact still remains that defect inspection should be done at the same AOI to produce an accurate defect map. In this context, accurate refers to the inclusion of printable defects only, whereas the non-printable defects would be omitted in the defect map as well. The second change brought about by the reflective geometry is the multi-layer itself. Imperfections in the layer thickness or the presence of particles will lead to variations in the optical path length and, therefore, a distorted wave-front, a so-called phase defect. Phase defects can lead to destructive interference and, thereby, print a non-existing structure or change patterns and, in the worst case, leading to short or open circuits in the finished device.

Patterned mask metrology is generally split into two disciplines: review and inspection. Whereas both can be carried out with coherent diffractive imaging (CDI), the requirements differ. In inspection, the full  $150 \times 150$  mm<sup>2</sup> mask has to be scanned, which is only possible within an acceptable time frame if all elements of the measurement chamber are optimized for maximum throughput. This includes a fast stage, multi-kHz detector and also a powerful source that is able to deliver the flux necessary for the required short exposure times. In this review paper, we will omit the source discussion as it would be outside of the scope of the materials discussed and rather

focus on the algorithms side, to present the reader with the latest achievements in terms of resolution. In short, during inspection, the exact illumination conditions of the scanner need not be reproduced and it is sufficient if the incident illumination is actinic and coherent. The main criterion is throughput, as the full mask has to be scanned. During review, on the other hand, only a limited number of sites – subsequently identified by inspection – have to be processed. Here, however, the illumination conditions have to match exactly those of the scanner to be able to correctly gauge the impact of the defect that is being reviewed. In both cases, a reference is needed against which the measured data can be compared. This reference can be a known defect-free mask with the exact same layout as the mask that is being inspected or reviewed ('die-to-die') or it can be calculated from a direct simulation based on the mask layout ('die-to-database'). In both cases, an affine transformation can be found that maximizes the cross-correlation and maximizes the signal-to-noise ratio (SNR) for the defects present.

## 2 Coherent diffractive imaging and ptychography

In the last two decades, a new approach to x-ray microscopy called coherent diffractive imaging (or coherent diffraction imaging, coherent scattering microscopy, lensless imaging, CDI) has revolutionized the field [3]. CDI allows structure determination of arbitrary (non-crystalline) samples without the need for an objective lens. The complex amplitude of the sample is calculated from the measured diffraction. More precisely, when the sample is illuminated with coherent light, the resulting diffraction can be measured with a CCD (PI-MTE 2048B, Princeton Instruments) detector. During this process, the phase is lost, but it can be reconstructed using an iterative algorithm that takes as input the measured magnitude and a number of constraints [4, 5]. This method has been successfully applied [6] and extended to a wide range of samples and experimental setups.

In contrast to classical x-ray microscopes, which are limited in resolution mainly by the quality of the objective lens, CDI can achieve a diffraction-limited resolution. As a matter of fact, it has recently been shown that with a slight modification in the algorithm that employs a modulus constraint on the incident illumination, a resolution of 12.6 nm for a regular grating could be achieved [7]. Indeed, this is below the incident wavelength of 13.5 nm and close to the Abbe limit of 12.5 nm. While this method has enabled

a high-resolution lensless microscopy, it is still limited in its applicability, as one of the necessary constraints for a successful convergence of the algorithm is the existence of a finite support, which, in practice, means that the field of view is limited to a few micrometers.

There are many extensions to CDI, such as Bragg CDI, Fresnel CDI, and ptychographic CDI [3]. In ptychographic CDI – or ptychography – the finite support constraint of CDI can be lifted by scanning the sample, using overlapping positions of a finite spot size [8, 9]. The overlap provides redundancy in the data and allows the algorithm to reconstruct the complex amplitude of the incident illumination (*probe*) alongside the sample (*object*). The common steps to most ptychography implementations are:

1. generate an initial guess of the *probe* and *object*
2. propagate *probe* and *object* to the detector plane
3. replace calculated *object* magnitude with measured data
4. update *probe* and *object* complex amplitudes to minimize the difference obtained in the previous step
5. propagate back to *object* plane

Steps 2–5 are repeated until convergence is achieved. A handy error metric to gauge convergence is the difference between the calculated and measured sample amplitude. Next to the redundancy in the data, which is achieved by using partially overlapping positions, step 3 constitutes a second constraint that links the iteration to the measured data. Only the magnitude of the diffracted signal is accessible as the phase information cannot be recorded by a CCD camera.

CDI methods have a number of advantages over imaging with optics. Being lensless, they do not suffer from aberrations and depth-of-focus limitations inherent to objective lenses. Both amplitude and phase are extracted, whereas optics-based imaging requires through-focus imaging in order to reconstruct the phase. Nano-imaging with CDI is feasible and relatively simple in reflection mode. As both condenser optics and detector do not need to be very close to the sample, there is sufficient space for sample rotations. Because of these strengths, CDI methods, in general, and ptychography, in particular, have become wide-spread, and many groups have started applying them to EUV imaging and EUV mask inspection.

### 3 Blank defect inspection

Since in EUV masks the absorber pattern is fabricated on top of a reflective Mo/Si multi-layer structure, a new type of defect, the so-called phase defect, is commonly observed.

These defects generally stem from thickness variations in the multi-layer caused by trapped particles or bumps and pits in the underlying substrate. As the source of these defects originates from underneath the multi-layer, they are difficult to inspect by SEM, AFM or, in fact, any inspection method that can probe only the mask surface.

Analyzing a through-focus series gathered with the SEMATECH Berkeley Actinic Inspection Tool (AIT) with a modified Gerchberg-Saxton algorithm [4], researchers at the Lawrence Berkeley National Lab (LBNL) have been able to identify phase defects in patterned and blank EUV masks with a root mean square accuracy of down to 2 mrad [10]. This was the first application of a CDI method to analyze this elusive class of defects. Programmed phase defects have also been observed with the micro-coherent EUV scatterometry microscope (micro-CSM) at Hyogo, where ptychography was employed instead of CDI to get a quantitative reconstruction of the phase distribution across the aerial image [11].

Researchers at the RWTH Aachen have installed a Schwarzschild objective-based microscope, where phase defects can be identified without any need of image reconstruction [12, 13]. A similar approach has been followed by the industry with the development of the Lasertec Actinic Blank Inspection tool (ABI) [14, 15]. The ABI tool is jointly developed by EIDEC and imec. It is currently the most advanced tool available in terms of industrial integration. In a recent test, the SHARP actinic microscope was used to validate the predictability of actinic mask inspection for defect printability [16]. The results demonstrated the feasibility of the chosen method and, in the future, will enable defect-free printability in high-volume manufacturing.

## 4 Mask defect inspection in periodic patterns

### 4.1 Coherent diffractive imaging

In 2009, researchers at the university of Hyogo installed a coherent EUV scattering microscope (CSM) at the NewSUBARU synchrotron facility. Initially, the CSM used CDI to reconstruct gratings and hole patterns using Fienup's hybrid input-output algorithm [5, 17]. Broadband light provided by a bending magnet source was passed through a 5  $\mu\text{m}$  diameter pinhole and a 200 nm-thick Zr filter to reduce and partially monochromatize the incident beam. The resulting beam was then collimated by a spherical Mo/Si multi-layer mirror and brought onto the mask at a 6° angle. Through the use of a high-harmonic generation

source, the power on mask was increased by four orders of magnitude from  $\sim 1$  pW to  $\sim 10$  nW [18], and the exposure time could be further reduced by the implementation of a single-mirror setup in the branching chamber that separates EUV light from that of the Ti:Sapphire pumping laser [19]. A  $2048 \times 2048$ -pixel CCD camera recorded the far-field diffraction image with a numerical aperture (NA) of  $\approx 0.15$ , corresponding to a maximum resolution of  $\approx 90$  nm. Using TaN absorber patterns on a multi-layer mask substrate, a 100 nm hp grating was resolved.

A similar chamber is also installed at the RWTH Aachen, where the amplitude and phase reconstruction of a sample using a compact incoherent gas-discharge-produced plasma source was shown for the first time [20]. The achieved spatial resolution for an incident wavelength of 17.3 nm – corresponding to the oxygen emission line – was estimated to be  $160 \pm 40$  nm. The pinch plasma emits multiple sharp emission lines in a wide spectral band ranging from EUV to visible light. A specific frequency can be chosen by applying a spectral filter. The experiment shown here used a transmission mask fabricated by focused ion beam milling, but the chamber could be refitted to work in reflection mode as well.

## 4.2 Scanning scattering contrast microscopy

CDI, and even more so, ptychography, are excellent methods for EUV mask defect inspection. However, as they rely on iterative solutions of the phase problem, they are computationally expensive. To isolate defects in periodic structures, it is also possible to employ a more direct method called scanning scattering contrast microscopy (SSCM) that requires no aerial image reconstruction and only takes diffraction data as input [18, 19, 21–25]. Strictly speaking, this is not a CDI method as no imaging is being done, but we nevertheless feel that it deserves mentioning in this overview as it potentially provides a method of interest for inspection. Because of the minimal requirements in terms of computation, the high throughput required by the industry can be reached when appropriate stage and detector are being used.

A regular, periodic pattern such as a grating or a hole array exhibits strongly localized diffraction peaks akin to Bragg peaks in crystallography [6]. Any irregularity in one of these structures can be considered a break of symmetry and will show up in the diffraction image as diffuse scattering. Through subtraction of the measured diffraction patterns from another set of diffraction patterns gathered either at a reference site with known non-defective structures or calculated by simulating the EUV light

propagation through the mask layout, a defect map can be computed.

The diffraction pattern intensity of a defect-free mask can be expressed by [24]:

$$I_R(\xi_x, \xi_y) = |\mathcal{F}[O(x, y)P(x, y)]|^2 \quad (1)$$

where  $\mathcal{F}$  denotes the Fourier transform operator, and  $O(x, y)$  and  $P(x, y)$  stand for the two dimensional complex amplitude of the mask pattern reflection and the incident illumination, respectively.  $O(x, y)$  is also dependent on the wavelength of the incident light and the angle of illumination. If the structure that is illuminated includes a defect, it will alter the mask pattern reflection.

$$I(\xi_x, \xi_y) = |\mathcal{F}\{[O(x, y) + \varepsilon(x, y)]P(x, y)\}|^2 \quad (2)$$

Because of the linearity of  $\mathcal{F}$ , this can be expanded into:

$$I(\xi_x, \xi_y) = |\mathcal{F}[O(x, y)P(x, y)] + \mathcal{F}[\varepsilon(x, y)P(x, y)]|^2 \quad (3)$$

Using  $Ae^{i\alpha} = \mathcal{F}[O(x, y)P(x, y)]$  and  $Be^{i\beta} = \mathcal{F}[\varepsilon(x, y)P(x, y)]$ , equation (3) can be rewritten as:

$$I(\xi_x, \xi_y) = A^2 + 2AB\cos(\alpha - \beta) + B^2 \quad (4)$$

The subtraction of the signal from the defect-free pattern by that from the defective pattern can then be expressed by:

$$I - I_R = AB\cos(\alpha - \beta) + B^2 \quad (5)$$

where the cross-product is an interference term, and the defect signal is given by  $B^2$ . As the scattering of the defect is relatively weak compared to the main diffraction orders of the periodic mask pattern, the major contribution to the

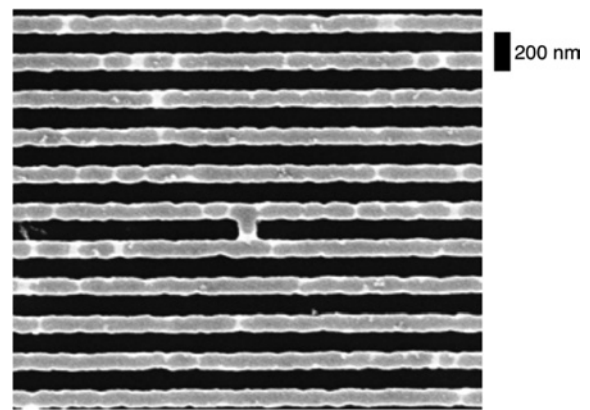


**Figure 1:** SEM micrograph of a 100 nm hp grating with a  $100 \times 100$  nm<sup>2</sup> programmed bridge defect on a Mo/Si multi-layer mask. The absorber was patterned from 40 nm-thick Ni using a lift-off process. The sample exhibits a large LER, and several unprogrammed defects are visible.

signal difference is due to the interference term. Using a 100 nm hp grating sample with a 100 nm<sup>2</sup> bridge defect (cf. Figure 1), a defect map could be obtained despite the very high absorber roughness and the presence of several unprogrammed defects as shown in Figure 2. This sample was fabricated at the Paul Scherrer Institut (PSI) using a non-optimized lift-off process, which led to the large line-edge-roughness (LER). In case of a CD error (i.e. one line of different width in an otherwise perfect grating), the diffuse signal of the defect is less localized and will, therefore, have a suitable SNR even for very small errors. An example is presented in Ref. [18], where the defect signal of a 2 nm CD error in an 88 nm hp grating can be distinguished clearly from the signal of the defect-free grating.

It was shown in simulations [21, 22] that the defect signal SNR is far above the scattering background from the expected LER and, especially in the case of periodic structures, relatively independent of the relative alignment of the defective and reference pattern positions. The simulation was carried out for a wide range of defects in hole patterns of nodes 10, 7, and 5, corresponding to a hp of 92 nm, 64 nm, and 44 nm on the mask, respectively.

## 5 Mask defect inspection in non-periodic patterns

In Section 4, we took an in-depth look at two methods that could be used for the inspection of periodic samples such as gratings or hole arrays, namely, CDI and SSCM.

Naturally, not all masks will consist of periodic structures, and a valid inspection method must also be provided for arbitrary patterns exhibiting no short-range periodicity. SSCM is a convenient and computationally cheap method to find defects in patterns, provided that a sufficient defect signal SNR can be achieved. While the diffraction peaks are relatively independent of pattern shifts for periodic samples, this is no longer true for arbitrary sample patterns where even small positioning errors on the nanometer scale will introduce new spatial frequencies that severely limit the achievable SNR. Therefore, this method requires an ultra high-precision sample stage. Also, for die-to-database comparison, a rigorous simulation of the mask design is required for an accurate modeling of the sample image. In contrast, die-to-die comparison is somewhat simpler, but has not been demonstrated at the time of writing. With ptychography, on the other hand, the comparison to simulated data (die-to-database) or to a known defect-free sample (die-to-die) takes place in real space where sub-pixel image registration is possible [26]. Ptychography and SSCM can both be applied to the same set of diffraction patterns as there is no difference in terms of data requirements.

Some preliminary results were shown using the CSM chamber described above, where a 2  $\mu\text{m}$  cross pattern was reconstructed with two different ptychographical reconstruction algorithms, one with and one without simultaneous retrieval of the incident illumination (cf. Figure 3) [27]. The dataset consisted of 36 diffraction patterns, taken with a step size of 2  $\mu\text{m}$ . The probe size was 5  $\mu\text{m}$  in diameter. In a more recent experiment, with increased

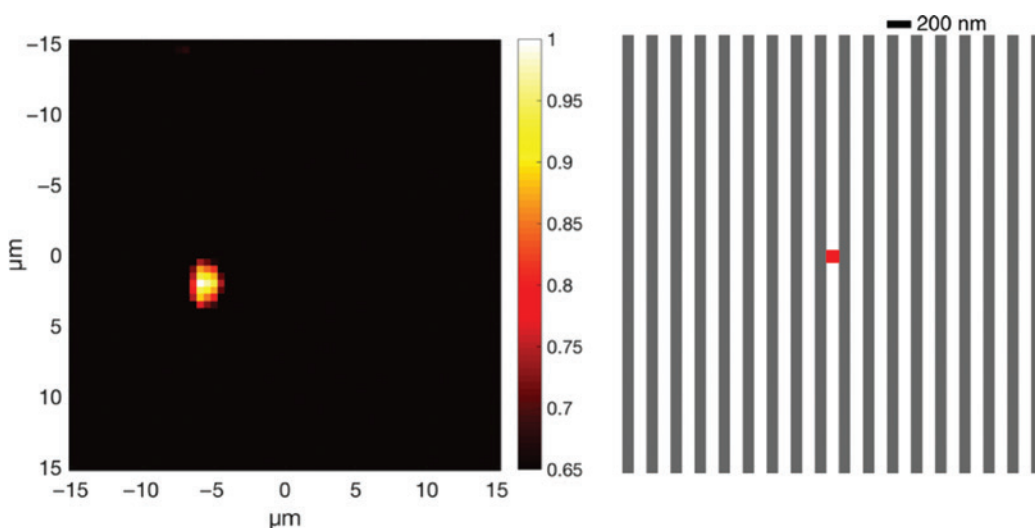


**Figure 2:** Example result obtained with our SSCM method from a 100 nm hp grating sample with a 100 nm bridge defect. (A) The defect map obtained from the sample shown in Figure 1. The SNR was  $\approx 7$ . (B) schematic layout of the measured sample. For easier localization, the layout was repeated periodically over an area of  $2 \times 2 \text{ mm}^2$ .

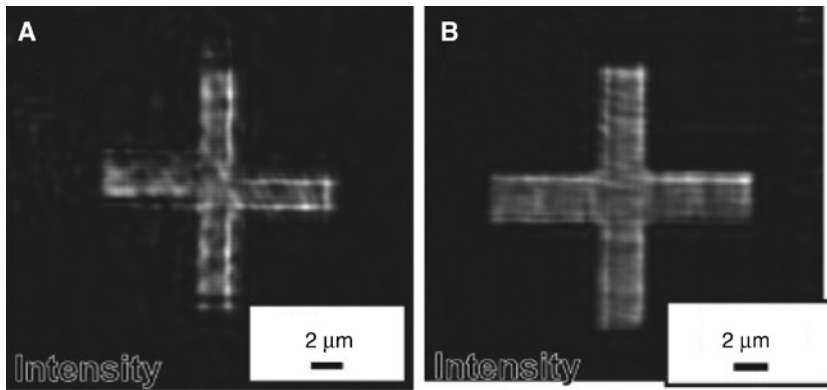


**Figure 3:** Reconstructed image of a 2  $\mu\text{m}$  cross pattern by two different ptychographical algorithms. (A) Without probe reconstruction. (B) With probe reconstruction. Copyright (2013) The Japan Society of Applied Physics.

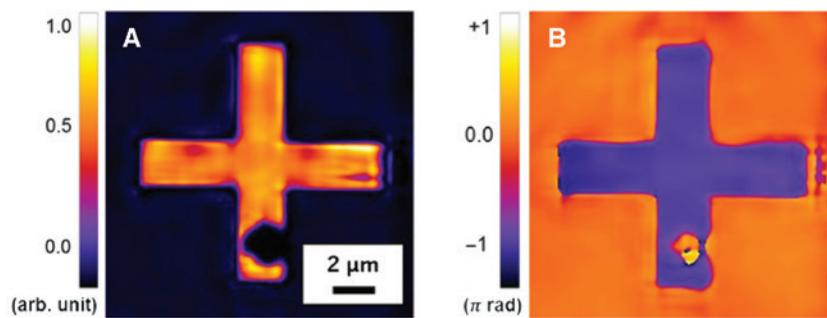


**Figure 4:** Improved reconstruction of a 2  $\mu\text{m}$  cross pattern with smooth background. (A) Magnitude. (B) Phase. Copyright (2017) The Japan Society of Applied Physics.

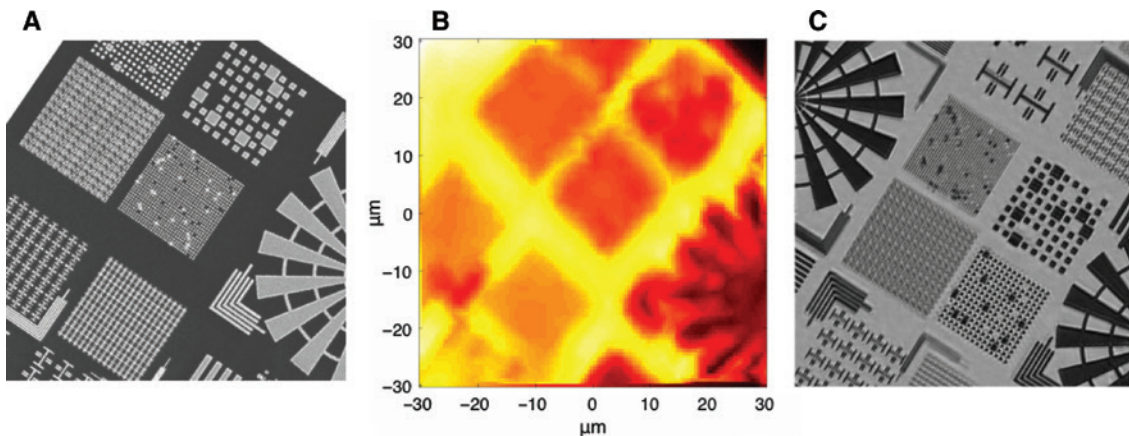


**Figure 5:** (A) SEM micrograph of the test sample. (B) Low-resolution map extracted from the 0th order of the recorded diffraction patterns. (C) Ptychography reconstruction.

source and stage stability, the reconstruction quality could be improved (cf. Figure 4) [28]. With the same setup, an 88 nm grating could be resolved.

Ptychographic reconstruction was also demonstrated using a partially coherent gas-discharge plasma source where a lateral resolution of  $255 \pm 10$  nm could be achieved [29]. Because of the low photon count, each

scan position had to be exposed for 30 s, leading to a total exposure time of 45 min. While both mentioned setups employ a standalone source, the long exposure time due to insufficient photon flux hinders their usability as mask inspection tools. A similar approach is being undertaken by the RESCAN project at the PSI, where a chamber closely resembling that of CSM was installed at the XIL-II

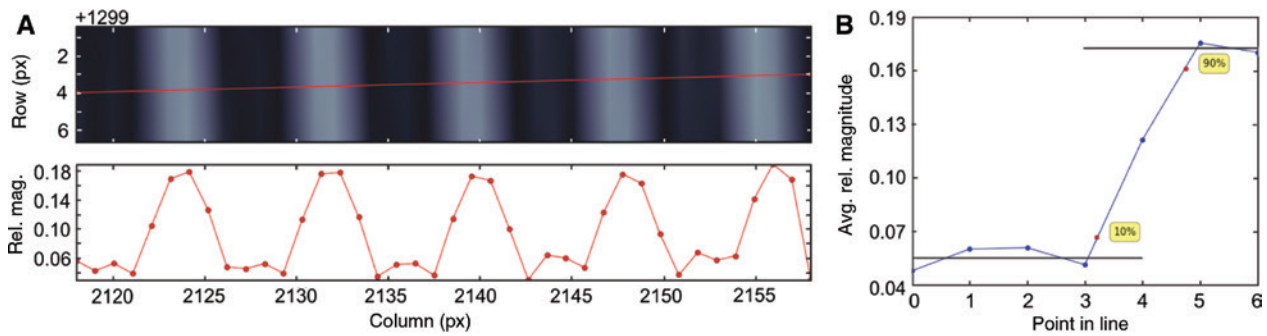


**Figure 6:** The 10–90% edge response of a 100-nm hp grating. (A) Close-up view of five lines from the grating (top) and the corresponding cross section (bottom); (B) The 10–90% edge response averaged over five lines. Each line consists of eight points, and the average of the first seven is shown here.

beamline of the Swiss Light Source synchrotron [21–25, 30]. The main difference lies in the source power and the employed algorithms. RESCAN uses the difference map [8] with a diverse-probe enhancement similar to that of Ref. [31], but with no adverse effect on the computation time in exchange for a heavier memory use. Also, the ability to mitigate decoherence effects due to the fluctuations of the source or sample vibrations was included [32]. Combined with multiple exposures of the same position using different exposure times to increase the dynamic range of the CCD, a resolution of about 50 nm could be reached, as shown in Figures 5 and 6 [30].

## 6 Wafer inspection

The favored method for high-resolution wafer inspection is the sequential application of focused ion beam (FIB) milling and SEM. The structure is milled down layer by layer via FIB and then imaged by SEM. A 3D rendering of the wafer structures can then be produced by combining all images, resulting in a high lateral resolution. The vertical resolution is generally lower, which is an effect of non-uniformity of the ion beam milling. The non-uniformity is more pronounced in areas where materials of different densities are present as they will be milled at different speeds. A new method called ptychographic X-ray computed tomography (PXCT) has been developed, which can image 3D samples in a non-destructive way [33]. PXCT has been developed by the cSAXS group at PSI, and they have recently applied it to image a section of an Intel Pentium G3260 CPU [34]. For this, a  $\approx 10\text{-}\mu\text{m}$  diameter cylinder was milled out of the chip and then imaged with 6 keV hard x-ray light at various angles. The contrast was high enough so that different materials could be discerned, and the final resolution was an unprecedented 14.6 nm in all

dimensions (cf. Figure 7). This result shows that ptychography at hard x-rays is extremely versatile and can be applied to a wide range of problems successfully.

A major problem of CDI methods at hard x-ray wavelengths is the need to thin down the wafer or cut out a certain section to enable sufficient transmission. If only surface information is needed, this could be avoided in a reflective setup. However, hard x-rays are reflected only at very low grazing angles. The reflectivity of all materials decreases sharply above the critical angle, which, in a very rough approximation, can be given by  $\theta_{\text{crit}}[\text{deg}] \approx \lambda[\text{nm}]$ . Thus, EUV enables higher angles than shorter wavelengths and, therefore, simpler reflection setups are possible. Additionally, the critical angle strongly depends on material properties, and by careful selection of the energies and reflection angle, one can obtain a high contrast between different materials.

Such an experiment was conducted by researchers from JILA, where they used their higher-harmonics generation source at 29.5 nm (27th harmonic) to illuminate a non-multilayer mask consisting of a Si substrate and a Ti absorber pattern [35]. The illumination angle was set to  $45^\circ$ , and they used tilted plane correction to remap the diffraction patterns onto a grid that is linear in spatial frequencies, in order to apply ptychography and the inherent Fourier transforms for reconstruction. Using only the relative phase change, they were able to accurately recover the height of the absorber pattern with results similar in quality to those gained from AFM. With the same chamber, but using CDI and a transmission setup, a resolution of 22 nm was achieved [36]. A different approach was taken by researchers at the ARCNL Laser-Lab, Amsterdam. They were able to use the whole emission spectrum of their HHG source by the application of a multi-wavelength iterative phase retrieval and, thereby, increase their resolution while minimizing the exposure time [37].

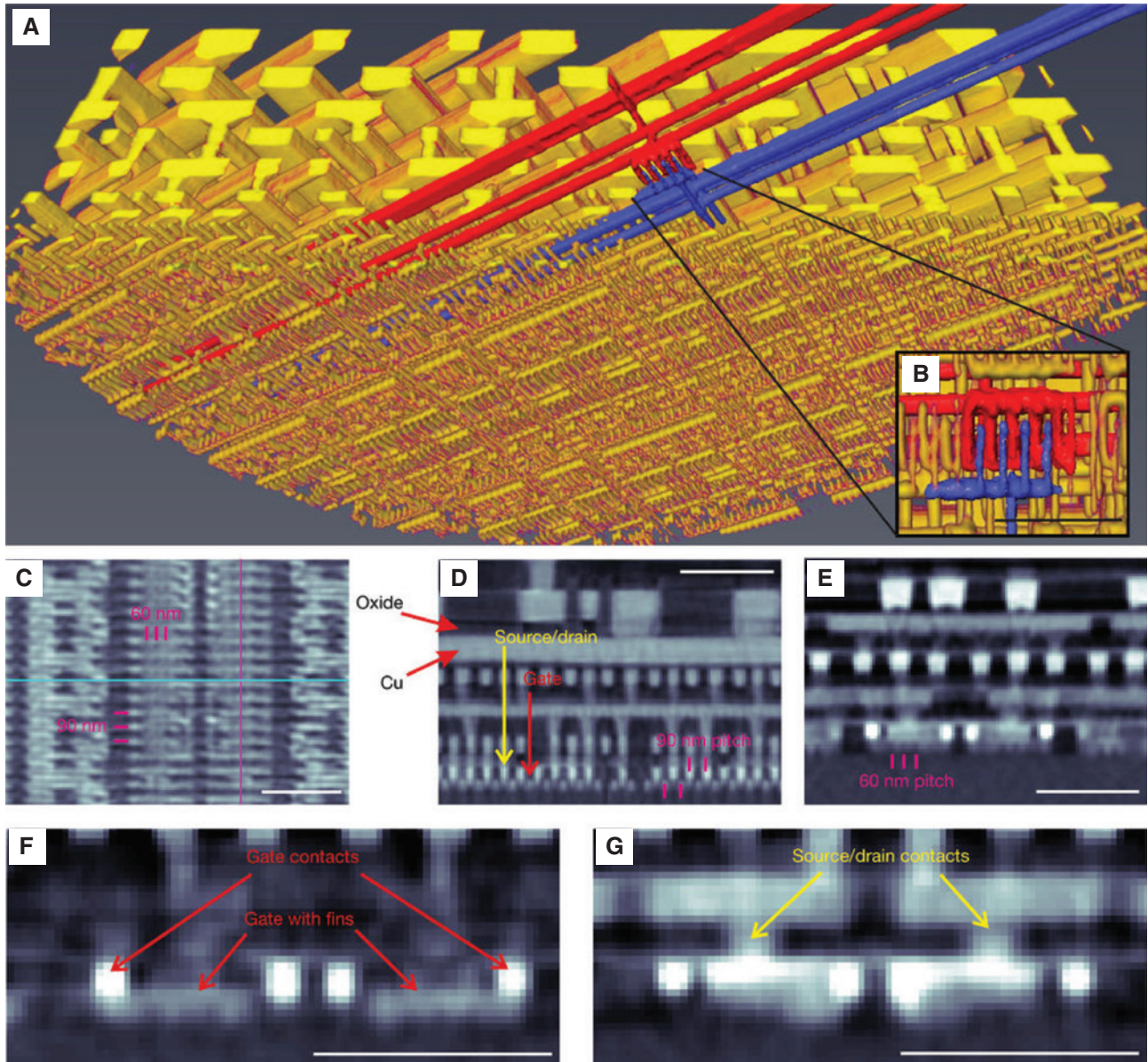


**Figure 7:** A 3D reconstruction of an Intel Pentium G3260 chip. (A) Segmented region of the full reconstruction showing fine details. (B) Close up view. (C) A 2D slice of the reconstruction, parallel to the chip surface. (D) A 2D slice orthogonal to the one shown in (C), taken along the purple line. (E) Sagittal slice, orthogonal to those shown in (C) and (D). (F, G) The 2D slices in the same direction as (E), showing a zoomed view. All scale bars represent 500 nm. Reprinted by permission from Macmillan Publishers Ltd: Nature [34], copyright (2017).

## 7 Conclusions and outlook

The CDI methods hold great promise for semiconductor manufacturing where new metrology approaches are in high demand in order to facilitate future progress. As mentioned above, one of the major challenges of EUVL for integration into high-volume manufacturing is the absence of a reliable patterned mask inspection tool providing sufficient resolution, sensitivity, and throughput for industrial viability. Although the demonstrated results

of various groups working in this field are very promising, there are yet many obstacles to overcome. As mentioned above, we have to make a distinction between review and inspection. While the former is tasked with identifying a small number of defects in known locations at great accuracy and under the same illumination conditions as those used for illuminating the wafer, inspection needs to process the full mask, locate and identify defects. To do this within an acceptable time-range, improvements in the detector are also necessary. As an example, let us take

a closer look at what is required to inspect a patterned mask area of  $100 \times 100 \text{ mm}^2$  within 5–10 h. If we assume a feasible probe size of  $30 \text{ }\mu\text{m}$  and a minimal overlap of 50%, which is necessary for a successful ptychographic reconstruction, millions of diffraction patterns have to be handled during this time, and the total data would amount to approximately 300 terabytes. One of the main bottlenecks in the processing pipeline is the limited speed of the currently available CCD detectors, which use up to 10 s to save a single image. For this reason, PSI is developing a hybrid silicon detector with a high dynamic range of  $\approx 10^6$  and a 2 kHz frame-rate for EUV and soft x-ray applications [24, 25, 38].

To maximize the photon flux and minimize the exposure time while being able to keep the NA-limited resolution, a high-throughput tool needs a high-brightness EUV source. This can easily be provided by any of the third-generation synchrotrons currently in use at research facilities around the world, but is not a viable option for a semiconductor fab. A more compact alternative is offered by the aforementioned HHG sources that have very high brightness. Unfortunately, only a fraction of the total flux available can be used due to the stringent requirement for a monochromatic beam at EUV wavelength, which limits the flux delivered by such a system to about  $1 \text{ }\mu\text{W}$ , yielding required exposure times of several seconds per frame.

One way to deliver the necessary flux, but keep the source reasonably small, is the recently proposed compact EUV source based on established accelerator technology currently under investigation at PSI [25]. Its conceptual design shows that a stable EUV power of  $\approx 100 \text{ mW}$  and a brightness of  $\approx 5 \text{ GW}/(\text{mm}^2 \text{ sr})$ , while the footprint can be limited to  $12 \times 5 \text{ m}^2$ , are feasible.

A further challenge in terms of both hard- and software is the improvement of algorithms that need to be able to handle and analyze the massive amounts of data arriving with a multi-kHz frame-rate detector within the time-frame of a few hours. Furthermore, the CDI and ptychography results presented in this paper were all acquired with a step-and-go scan method. For high-throughput mask scanning, stage movement will have to be continuous, thereby introducing a coherence loss into the diffraction patterns similar to what would be expected from sample vibrations. Using a novel concept called fly-scan ptychography, the elongated probe arising from continuous movement can be deconvolved into separate eigenstates, thus allowing an accurate reconstruction of the sample [39]. The demonstrated concepts and results using CDI for mask and wafer metrology are very encouraging, and with further developments of the hardware

and software, CDI methods can provide viable solutions to the challenges in semiconductor manufacturing.

## References

- [1] K. A. Goldberg and I. Mochi, *J. Vac. Sci. Technol. B Nanotechnol. Microelectron.* 28, C6E1–C6E10 (2010).
- [2] I. Mochi, V. Philipsen, E. Gallagher, E. Hendrickx, K. Lyakhova, et al., *Proc. SPIE* 9776, 97761S (2016).
- [3] J. Miao, T. Ishikawa, I. Robinson and M. Murnane, *Science* 348, 530–535 (2015).
- [4] R. Gerchberg and W. Saxton, *Optik* 35, 237–246 (1972).
- [5] J. R. Fienup, *Opt. Lett.* 3, 27–29 (1978).
- [6] J. Miao, P. Charalambous, J. Kirz and D. Sayre, *Nature* 400, 342–344 (1999).
- [7] D. Gardner, M. Tanksalvala, E. Shanblatt, X. Zhang, B. Galloway, et al., *Nat. Photonics* 11, 259–263 (2017).
- [8] P. Thibault, M. Dierolf, A. Menzel, O. Bunk, C. David, et al., *Science* 321, 379–382 (2008).
- [9] A. Maiden and J. Rodenburg, *Ultramicroscopy* 109, 1256–1262 (2009).
- [10] I. Mochi, K. A. Goldberg and S. Huh, *J. Vac. Sci. Technol. B* 28, C6E11–C6E16 (2010).
- [11] T. Harada, H. Hashimoto, T. Amano, H. Kinoshita and T. Watanabe, *J. Micro Nanolithogr. MEMS MOEMS* 15, 021007 (2016).
- [12] A. Maryasov, S. Herbert, L. Juschkina, R. Lebert and K. Bergmann, *Proc. SPIE* 7985, 79850C–79850C–8 (2011).
- [13] L. Bahrenberg, S. Herbert, J. Tempeler, A. Maryasov, O. Hofmann, et al., *Proc. SPIE* 9422, 942229–942229–9 (2015).
- [14] R. Jonckheere, D. Van den Heuvel, N. Takagi, H. Watanabe and E. Gallagher, *Proc. SPIE* 9422, 942216–942216–10 (2015).
- [15] N. Takagi, H. Watanabe, D. Van den Heuvel, R. Jonckheere and E. Gallagher, *Proc. SPIE* 9658, 96580F–96580F–6 (2015).
- [16] P. Mangat, E. Verduijn, O. R. Wood, M. P. Benk, A. Wojdyla, et al., *Proc. SPIE* 9658, 96580E–96580E–8 (2015).
- [17] T. Harada, J. Kishimoto, T. Watanabe, H. Kinoshita and D. G. Lee, *J. Vac. Sci. Technol. B* 27, 3203–3207 (2009).
- [18] M. Nakasuji, A. Tokimasa, T. Harada, Y. Nagata, T. Watanabe, et al., *Jpn. J. Appl. Phys.* 51(6S), 06FB09 (2012).
- [19] T. Fujino, Y. Tanaka, T. Harada, Y. Nagata, T. Watanabe, et al., *Jpn. J. Appl. Phys.* 54(6S1), 06FC01 (2015).
- [20] J. Bußmann, M. Odstrčil, R. Bresenitz, D. Rudolf, J. Miao, et al., *Proc. SPIE* 9589, 95890L–95890L–8 (2015).
- [21] I. Mohacsi, P. Helfenstein, R. Rajendran, and Y. Ekinci, *Proc. SPIE* 9778, 977810 (2016).
- [22] Y. Ekinci, P. Helfenstein, R. Rajeev, I. Mochi, I. Mohacsi, et al., *Proc. SPIE* 9985, 99851P–99851P–9 (2016).
- [23] P. Helfenstein, I. Mochi, R. Rajendran, S. Yoshitake and Y. Ekinci, *Proc. SPIE* 10143, 101431Q–101431Q–7 (2017).
- [24] I. Mochi, P. Helfenstein, I. Mohacsi, R. Rajeev, D. Kazazis, et al., *J. Micro Nanolithogr. MEMS MOEMS* 16, 041003 (2017).
- [25] R. Rajendran, I. Mochi, P. Helfenstein, I. Mohacsi, S. Redford, et al., *Proc. SPIE* 10145, 101450N–101450N–12 (2017).
- [26] M. Guizar-Sicairos, S. T. Thurman and J. R. Fienup, *Opt. Lett.* 33, 156–158 (2008).

- [27] T. Harada, M. Nakasuji, Y. Nagata, T. Watanabe and H. Kinoshita, *Jpn. J. Appl. Phys.* 52(6S), 06GB02 (2013).
- [28] D. Mamezaki, T. Harada, Y. Nagata and T. Watanabe, *Jpn. J. Appl. Phys.* 56(6S1), 06GB01 (2017).
- [29] M. Odstrčil, J. Bußmann, D. Rudolf, R. Bresenitz, J. Miao, et al., *Opt. Lett.* 40, 5574–5577 (2015).
- [30] P. Helfenstein, I. Mohacsi, R. Rajeev and Y. Ekinci, *J. Micro Nanolithogr. MEMS MOEMS* 15, 034006 (2016).
- [31] M. Odstrčil, P. Baksh, S. A. Boden, R. Card, J. E. Chad, et al., *Opt. Express* 24, 8360–8369 (2016).
- [32] P. Thibault and A. Menzel, *Nature* 494, 68–71 (2013).
- [33] M. Dierolf, A. Menzel, P. Thibault, P. Schneider, C. M. Kewish, et al., *Nature* 467(7314), 436–439 (2010).
- [34] M. Holler, M. Guizar-Sicairos, E. H. Tsai, R. Dinapoli, E. Muller, et al., *Nature* 543, 402–406 (2017).
- [35] M. D. Seaberg, B. Zhang, D. F. Gardner, E. R. Shanblatt, M. M. Murnane, et al., *Optica* 1, 39–44 (2014).
- [36] M. D. Seaberg, D. E. Adams, E. L. Townsend, D. A. Raymondson, W. F. Schlotter, et al., *Opt. Express* 19, 22470–22479 (2011).
- [37] S. Witte, V. T. Tenner, D. W. E. Noom and K. S. E. Eikema, *Light Sci. Appl.* 3, e163 (2014).
- [38] A. Mozzanica, A. Bergamaschi, S. Cartier, R. Dinapoli, D. Greiffenberg, et al., *J. Instrum.* 9, C05010 (2014).
- [39] X. Huang, K. Lauer, J. N. Clark, W. Xu, E. Nazaretski, et al., *Sci. Rep.* 5, 9074 (2015).